

# 1 Emergence of metabolic landscapes in yeast monolayer colonies

2 Zoran S Marinkovic<sup>1,2,3</sup>, Clément Vulin<sup>1,4,5</sup>, Mislav Acman<sup>1,3</sup>, Xiaohu Song<sup>2</sup>, Jean Marc Di  
3 Meglio<sup>1</sup>, Ariel B. Lindner<sup>\*,2,3</sup>, Pascal Hersen<sup>\*,1</sup>

4  
5 <sup>1</sup>Laboratoire Matière et Systèmes Complexes, UMR 7057 CNRS & Université Paris Diderot, 10 rue Alice Domon et  
6 Léonie Duquet, 75013 Paris, France.

7 <sup>2</sup>U1001 INSERM, 24 Rue du Faubourg St Jacques, 75006, Paris, France.

8 <sup>3</sup>CRI, Université Paris Descartes, 8-10 Rue Charles V, 75004, Paris, France.

9 <sup>4</sup>Institute of Biogeochemistry and Pollutant Dynamics, ETH Zurich, Zurich, Switzerland.

10 <sup>5</sup>Department of Environmental Microbiology, Eawag, Dübendorf, Switzerland.

11  
12 \*Correspondence and requests for materials should be addressed to Ariel Lindner ([ariel.lindner@inserm.fr](mailto:ariel.lindner@inserm.fr)) or Pascal  
13 Hersen ([pascal.hersen@univ-paris-diderot.fr](mailto:pascal.hersen@univ-paris-diderot.fr)).

14  
15 **Keywords:** Yeast colony, Microfluidics, Gene expression, Spatial Organization, Metabolism.

## 16 Abstract

17 Microbial colonies are fascinating structures in which growth and internal organization reflect the  
18 morphogenesis of complex spatiotemporal processes. However, there is no global understanding of how  
19 metabolic interactions between cells affect the internal structure of microbial colonies. Here, we generated  
20 long arrays of monolayer yeast colonies within a multi-layered microfluidic device perfused from only one  
21 side to study gradient formation and microbial colony dynamics within defined boundary conditions. We  
22 observed the emergence of stable glucose gradients using fluorescently labelled hexose transporters and  
23 quantified the spatial correlations with intra-colony growth rates and expression of other genes regulated  
24 by glucose availability. These landscapes depended on the external glucose concentration as well as  
25 secondary gradients, *e.g.*, amino acid availability. This work demonstrates the regulatory genetic networks  
26 governing cellular physiological adaptation are the key to internal structuration of cellular assemblies. This  
27 approach could be used in the future to decipher the interplay between long-range metabolic interactions,  
28 cellular development and morphogenesis in more complex systems.

29

## 30 Introduction

31 Structured cellular communities are complex, dynamic systems and their composition, expansion and  
32 internal structure are the result of interactions between the cells and their microenvironment. Cells absorb  
33 and metabolize nutrients and also produce and secrete metabolites, creating spatial gradients of nutrients  
34 and metabolites. Thus, the cells at the outskirts of a multicellular assembly do not experience the same  
35 microenvironment as the cells deeply buried within. In turn, cellular physiology is dependent on the cell's  
36 position within a colony. Such variations in cellular physiology are consistently observed in a variety of  
37 multicellular systems – from bacterial and yeast colonies<sup>1,2</sup> to biofilms<sup>3</sup> and tumours<sup>4,5</sup> – and are reflected  
38 by altered gene expression levels and cellular phenotypes such as specific growth rates, nutrient uptake  
39 rates and metabolic activity. Such variations presumably emerge as a result of long-range metabolic  
40 interactions between cells, in that the cellular microenvironment at one position depends on the nutrient  
41 uptake rate at another position.

42  
43 Notably, multicellular communities<sup>6-8</sup> exhibit various adaptive benefits, including higher cell proliferation,  
44 improved access to resources and niches<sup>9</sup>, collective defence (*e.g.*, against antagonists, drugs, antibiotics)<sup>3</sup>  
45 and optimization of population survival when confronted with diverse physical, chemical, nutritional or  
46 biological challenges<sup>10</sup>. These examples indicate that understanding the emergence and maintenance of  
47 complex spatial multicellular structures is important from ecological<sup>11-13</sup>, medical<sup>14-16</sup> and evolutionary<sup>17-</sup>  
48 <sup>19</sup> perspectives. Yet, despite the obvious contrast between homogeneous environments and the pronounced  
49 environmental heterogeneity of microbial cellular assemblies, the majority of scientific research to date has  
50 either focused on single cells in homogeneous environments or populations of cells grown in batch or  
51 continuous liquid cultures, and ignored the spatial complexity of structured multicellular communities.

52  
53 Given the massive knowledge accumulated on gene regulatory networks within single-cell conditions, it is  
54 tempting to try to reconstruct the emergence of gene expression landscapes on a global scale (*e.g.*, within  
55 structured communities) from local (*e.g.*, single cell) properties. However, the variations in the  
56 microenvironment within a multicellular assembly and their interconnections with gene expression and cell

57 metabolism are not known. Additionally, direct observation of three-dimensional colonies is cumbersome  
58 and often constrained by existing technologies. For example, two-photon microscopy of sliced agarose-  
59 encapsulated yeast colonies was required to show that yeast cells adopt different physiologies – and possibly  
60 different cell types – depending on their position within a colony<sup>2</sup>. Such complex methodologies are not  
61 amenable to time-lapse imaging, thus the temporal variations in gene expression and growth rates of single  
62 cells could not be discerned. As a result, experimental capacity limits our ability to observe the dynamics  
63 of colony morphogenesis and maturation. An alternative is to grow microbial cells in microfluidic devices  
64 to spatially constrain the growth of the cells and to control the delivery of nutrients<sup>20–24</sup>. Microfluidic  
65 experimental research is typically designed to ensure that the cells being studied experience a homogeneous  
66 environment as either completely independent single cells<sup>25,26</sup> or as a part of a small cell assembly<sup>27–29</sup>;  
67 however, such research does not capture emerging properties at a colony level, *i.e.* spatial variations in  
68 growth rates, microenvironments and phenotypes.

69  
70 In order to observe emerging properties at a colony level, we developed a microfluidic device to grow thin,  
71 extended arrays of yeast cell monolayers that are perfused with nutrients from one direction only. We  
72 demonstrate we could reproduce and quantify spatial variation in the cellular growth rate and the formation  
73 of gene expression landscapes for key metabolic genes involved in glucose transport and utilization.  
74 Interestingly, the gene expression landscapes exhibited a high degree of spatial correlation over a range of  
75 glucose concentrations. Notably, we show that an extended assembly of cells presents a spatial transition  
76 between fermentative (high glucose environment, fast growth, rapid glucose utilization) and respirative  
77 (low glucose environment, slow growth, slow but efficient glucose utilization<sup>30,31</sup>) regimes, located close  
78 to and far from the nutrient source, respectively. This spatial structure emerges from the interplay between  
79 how cells individually adapt to the microenvironment and, at the same time, alter their surroundings as a  
80 result of their metabolic activity.

## 81 Results

82 **Growing extended yeast monolayers.** Microfluidic systems are usually designed to ensure a homogeneous  
83 microenvironment for all cells<sup>20</sup>. In contrast, in this study, we designed a microfluidic device – dubbed the  
84 “yeast machine” – to grow long, narrow yeast monolayers with the aim of observing the emergence of  
85 nutrient gradients and spatial variations in cellular growth and gene expression landscapes. We used soft  
86 lithography techniques to fabricate a multi-layered microfluidic device composed of a large channel (to  
87 flow nutrients) and an array of perpendicular, extended (800  $\mu\text{m}$ -long), narrow (50  $\mu\text{m}$ -wide), flat (4.5  $\mu\text{m}$ -  
88 high) dead-end chambers in which yeast cells can grow as monolayers (Figure 1a, Supplementary Figure  
89 1). The length of the dead-end chambers was optimized to induce significant variations in the nutrient  
90 concentrations within the chambers due to cellular nutrient uptake (Figure 1a). The chamber width was  
91 large enough to avoid jamming during cell growth due to geometric constraints and small enough to avoid  
92 generation of complex, cell-recirculating flows induced by cell growth<sup>32</sup>. The chamber height was  
93 comparable to – but slightly larger than – the average size of a yeast cell, so the cells were vertically  
94 constrained to facilitate single-cell imaging and time-lapse fluorescence microscopy.

95  
96 The cells were injected into the main channel of the “yeast machine” and then forced into the dead-end  
97 chambers by centrifugation using a homemade 3D-printed holding device attached to a spin coater (see  
98 Supplementary Figure 1; Methods). The main channel was washed with yeast synthetic complete growth  
99 medium to remove excess cells; cells that were trapped in the dead-end chambers by centrifugation were  
100 not removed by the washing step. Nutrients were flowed through the main channel and could passively  
101 diffuse into the array of dead-end chambers. The cells formed growing monolayers that extended from the  
102 closed end of the chamber and collectively progressed towards the nutrient source (*i.e.* the open end of the  
103 chamber) as the cells pushed each other while growing (Figure 1a, b; Supplementary Movie 1). Cells  
104 eventually filled each chamber, forming an extended two-dimensional colony composed of about 2500 cells  
105 (Figure 1b), typically  $\sim 10$  cells wide and  $\sim 200$  cells long. Cells could be observed locally at high  
106 magnification (100 $\times$  objective), while the whole assembly could be seen at low magnification (10 $\times$   
107 objective). We recorded the cellular expansion and subsequent internal dynamics of these long monolayers,

108 as well as the landscape of expression of key fluorescently tagged endogenous genes, over time and over  
 109 an almost 1000-fold range of glucose concentrations (from 0.01% to 8% w/vol).

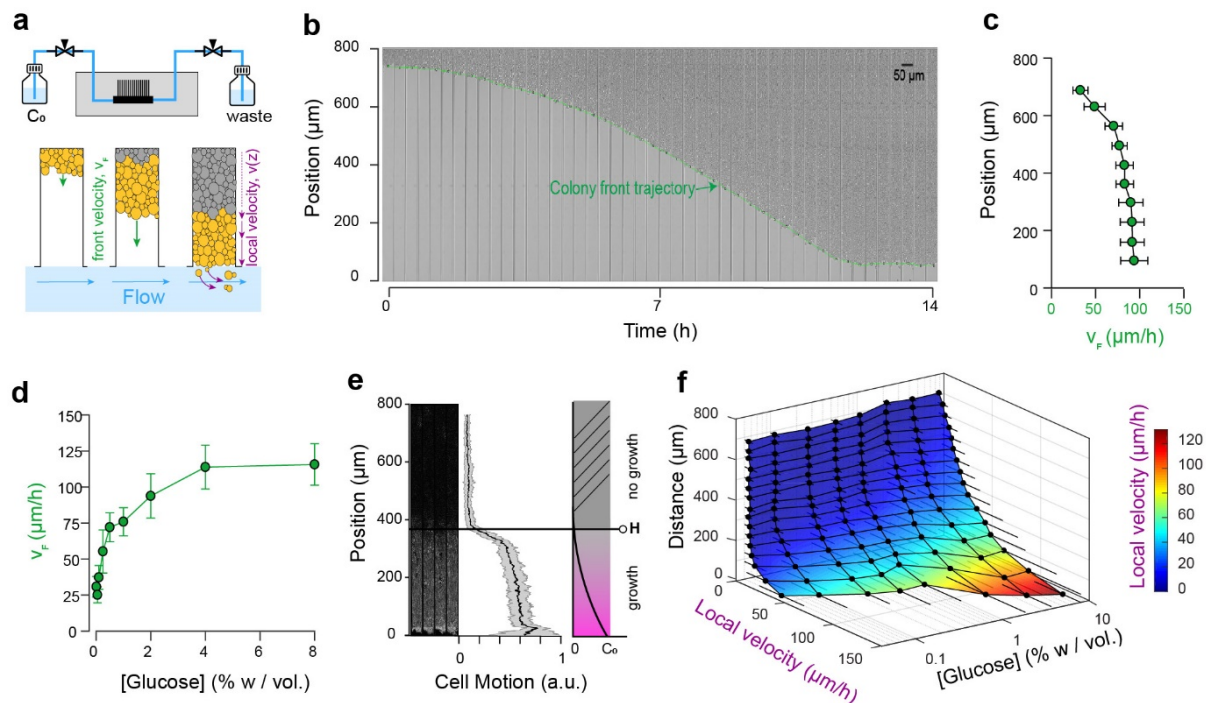


**Figure 1.** Expansion and dynamics of extended cellular monolayers. **1a.** The microfluidic device is perfused with nutrients using a pressure-driven system. Yeast cellular monolayers extend within the long chambers: front velocity ( $V_F$ ) and local velocity ( $V_Z$ ) are determined by cellular growth and division. **1b.** Example of a time-lapse collage of yeast monolayer expansion along an 800  $\mu\text{m}$ -long chamber (2% w/vol. glucose, 5 $\times$  amino acid concentration). Front velocity increases and reaches a plateau (indicated by flattening of the slope of the green curve). When the front approaches close to the open end of the chamber (*i.e.*, 0  $\mu\text{m}$ ), the over-spilling cells are constantly washed away by the nutrient flow within the main channel. **1c.** Front velocity reaches a maximum when the position of the front becomes close to the open end of the chamber indicating that after expanding by a typical distance ( $\sim 400$   $\mu\text{m}$  here for 2% w/vol. glucose), the maximal number of cells that receive glucose and can participate in expansion has been reached. 340 velocity data points binned into 10 equally spaced position points were extracted from  $n=12$  colony front trajectories (2% w/vol. glucose). The error bar denotes standard deviations of each bin ( $\sim 15$ -30 velocity data points). **1d.** Front velocity as function of external glucose concentration. Data comes from the bin closest to the open end of the chamber as measured in Figure 1c for each glucose concentration ( $n > 5$ ). Error bars denotes standard deviations. **1e.** Local cellular motion can be assessed by computing the standard deviation of pixel intensities across a stack of time-lapse images. Here, white areas indicate variations in movement across the time-lapse for cells below 400  $\mu\text{m}$ , while the cells above do not move. Averaging over several channels ( $n=9$ ), we obtained an indicator of cell motion and thus an estimate of the glucose penetration distance,  $H$  ( $\sim 400$   $\mu\text{m}$  for 2% glucose). **1f.** Local velocity decreases for cells deeper within the chamber. Local velocity also increases with external glucose concentration. Velocity Data, that were binned into 16 equally spaced position, comes from the analysis of  $>100$  cell trajectories. Error bars denote standard deviations.

110  
 111 **Cells collectively create, and experience, a spatially structured micro-environment.** Expansion of the  
 112 monolayers of cells was observed by microscopy at low magnification (10 $\times$  objective). Under standard  
 113 glucose-rich conditions (2% w/vol; 111 mM) and excess amino acids (5 $\times$  CSM, see *Methods*), the front  
 114 velocity,  $V_F$ , increased during the first 2-4 h and eventually reached a steady-state close to 100  $\mu\text{m}\cdot\text{h}^{-1}$

115 (Figure 1c, d, Supplementary Movie 1). Front velocity is the sum of the contribution of every cell to colony  
116 expansion. Therefore,  $V_F$  depends on the quantities of glucose and other nutrients that penetrate inside the  
117 yeast monolayer, which impact both the number of cells that grow and their growth rates. Initially, the  
118 monolayer is sparsely populated and sufficient glucose is expected to reach all cells. After growth and  
119 division, a larger number of cells can participate in global expansion of the population. Thus, the front  
120 velocity is expected to quickly increase over time. However, at some point, as the size of the monolayer  
121 increases, the cells close to the dead end of the chamber will stop growing (due to absorption and  
122 metabolism of available nutrients by cells closer to the nutrient source/chamber opening) and the front  
123 velocity will plateau. Hence, a steady-state is reached where a constant number of cells with access to  
124 glucose continue to divide and move passively towards the nutrient source, while the number of cells at the  
125 dead end of the chamber deprived of glucose (and other nutrients) remains unchanged. If we consider the  
126 ideal case in which yeast cells are 4  $\mu\text{m}$ -wide and divide every 90 min in the presence of glucose, each cell  
127 leads to an expansion of 4  $\mu\text{m}$  every 90 min, or 2.6  $\mu\text{m}\cdot\text{hr}^{-1}$ . The observed terminal front velocity of  $94 \pm 8$   
128  $\mu\text{m}\cdot\text{hr}^{-1}$  (Figure 1) can be attributed to the first  $36 \pm 3$  layers of cells, i.e. the first 140  $\mu\text{m}$  of the colony. The  
129 glucose penetration distance can be approximated by assuming<sup>1</sup> that glucose – of which the concentration  
130 is maintained at  $C_0$  at the front of the monolayer – freely diffuses within the assembly with a diffusion  
131 coefficient  $D \sim 100 \mu\text{m}^2\cdot\text{s}^{-1}$  and is absorbed by cells at a constant rate,  $q_0$ , of  $\sim 1 \text{ mM}\cdot\text{s}^{-1}$ . Diffusion law  
132 dictates that the glucose concentration is expected to decrease significantly after a typical distance,  $H$ , that  
133 scales with  $\sqrt{\frac{DC_0}{q_0}} \sim 100 \mu\text{m}$ . Our direct observation (Figure 1e) showed that for a layer of growing cells,  $H$   
134 is around 400  $\mu\text{m}$  at 2% w/v glucose. Notably, both estimations are in agreement, albeit they underestimate  
135 the observed size of the growing layer. These discrepancies result from discarding the decay in the cellular  
136 growth rate at decreasing glucose concentrations and the variation in the specific cellular uptake rate,  $q$ ,  
137 with glucose concentration. Indeed, the interplay between glucose diffusion and uptake is central to  
138 structuration of the colony as it affects both the number of cells that have access to glucose and the glucose  
139 concentration in the microenvironment of each region, and thus determines which cells actually participate  
140 in colony expansion and by how much<sup>1</sup>. The true glucose penetration distance is therefore likely to be larger  
141 than the ‘*guesstimate*’ above. Yet, inferring the true penetration distance would require a detailed model of



142 the dependency of both cellular glucose absorption and the growth rate on the glucose concentration, as  
143 well as experimental measurements of the glucose concentrations within the monolayer. This outlines the  
144 difficulty of predicting the internal structure of a simple yeast monolayer due to our limited understanding  
145 of how yeast cells interact with nutrients and the difficulty of obtaining quantitative details of the  
146 microenvironmental landscapes within a yeast monolayer. In the following text, we quantify the expression  
147 of different glucose concentration-dependent transporters as a possible proxy for intra-colony glucose  
148 concentration. We even ventured further, to study how landscapes of cellular growth and expression of key  
149 genes involved in glucose transport self-emerge from long-range metabolic interactions within the yeast  
150 colony.

151  
152 **Front velocity increases with glucose concentration.** Increasing the glucose concentration (from 0.01%  
153 to 8% *w/vol*) led to higher terminal front velocities (Figure 1d), in agreement with the fact that at higher  
154 concentrations, glucose will penetrate further by diffusion in the colony (Figure 1a). Thus, increasing the  
155 concentration allows a larger number of cells to access glucose and participate in the growth of the colony.  
156 Yet, the front velocity does not increase linearly with glucose concentration, and plateaus at very high  
157 glucose concentrations ( $> 4\%$  *w/vol*). One interpretation is that at this concentration range, sufficient  
158 glucose reaches the dead end of the chamber, allowing all cells to participate in the growth of the assembly.  
159 However, based on  $V_F \sim \mu L$ , where  $L$  is the length of the dead-end chamber and  $\mu$  is the average cell growth  
160 rate, one would expect a saturating front velocity of  $368 \mu\text{m}\cdot\text{h}^{-1}$ , much larger than the measured value of  
161  $100 \mu\text{m}\cdot\text{h}^{-1}$ .

162  
163 Glucose is not the only nutrient required for cellular growth; amino acids can be a limiting factor for  
164 auxotrophic strains such as the one employed in this study (S288C background). This is why we used an  
165 excess of amino acids ( $5\times$  CSM) compared to classic SC medium for yeast cell cultures. Indeed, using  
166 standard amino acid concentrations in the media resulted in significantly lower terminal front velocities,  
167 even at high glucose concentrations (Supplementary Figure 2). This suggests that amino acid availability  
168 can limit cellular growth, especially in the presence of high glucose concentrations, thereby leading to a



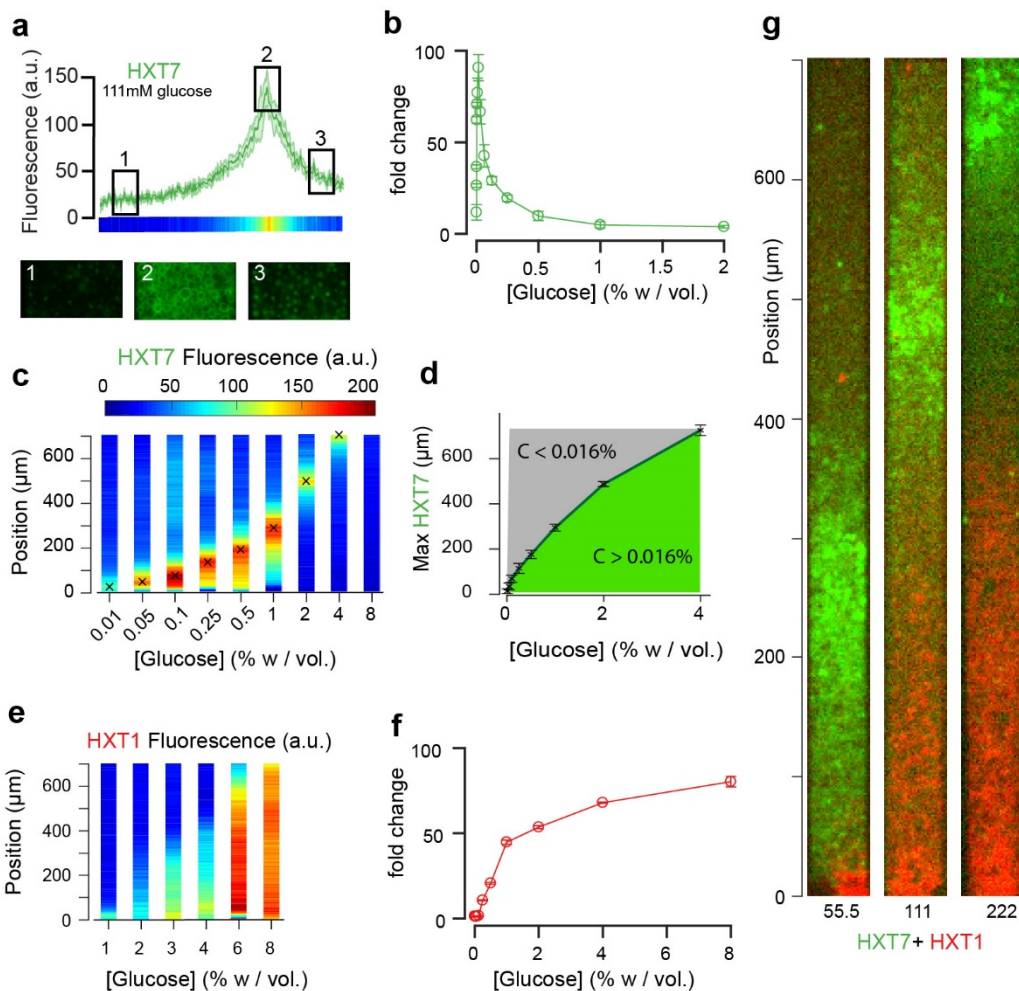
169 plateau in the terminal velocity (Figure 1d). As all experiments were performed under 5-fold higher amino  
170 acid concentrations than normal SC medium, other metabolites are likely to become rate-limiting for  
171 growth. Taken together, we conclude that the spatial variations in all metabolic components of the  
172 microenvironment need to be discerned in order to fully understand microbial colony growth. With that in  
173 mind, building a mathematical model to account for the observed expansion of a spatially structured colony  
174 is barely achievable, and we will not address this question here. Rather, we opted to further characterize the  
175 development of glucose gradients as a specific and critical component of the emergence of the metabolic  
176 landscape of the colony.

177  
178 **Local expansion rate decreases with distance from the nutrient source.** Once the dead-end chambers  
179 were filled with cells, we found the growth pattern was highly reproducible across parallel chambers at  
180 each glucose concentration. The cells closer to the open end of the chambers continued to divide, pushing  
181 cells out that were washed away by the flow in the nutrient channel. Cells closer to the dead end ( $y \sim 800$   
182  $\mu\text{m}$ ) did not move, grow nor divide. At standard glucose conditions (2% *w/vol*) and a high amino acid  
183 concentration (5 $\times$  CSM), significant cell motion was not observed after  $y \sim 400 \mu\text{m}$ , indicating very limited  
184 glucose is available to the cells that beyond this region. By tracking single cell trajectories, we measured  
185 the velocity field within the yeast monolayers over a range of glucose concentrations. We extracted > 100  
186 single cell trajectories per concentration, resulting in thousands of velocity data points (see *Methods*). As  
187 expected, increasing the glucose concentration in the nutrient channel (from 0.01% to 8% *w/vol*) led to  
188 higher local velocities deeper in the colony (Figure 1f, Supplementary Figure 3). Concomitantly, velocity  
189 also increased closer to the chamber opening when cells experienced a higher glucose concentration.

190  
191 In conclusion, our setup captures the essence of structured colonies, with the emergence of a landscape of  
192 growth divided into a non-growing area and actively growing area. This spatial separation is the result of  
193 the formation of glucose (and other nutrient) gradients. These gradients emerge as a result of cellular  
194 metabolic activity, which in turn affects the cellular growth rate and physiology at the local scale.

195

196 **Cellular metabolic activity creates gene expression landscapes.** The emerging glucose (and other  
197 nutrient) gradients are expected to both trigger and be governed by differential gene expression landscapes.  
198 To this end, we studied the expression of seven key glucose transporters (HXT1-7) whose expression is  
199 regulated by the extracellular glucose concentration. We employed yeast strains in which these endogenous  
200 glucose transporters were tagged with GFP (*Methods*), and recorded the fluorescence signals at the global  
201 scale using a low-magnification objective (10×) and local cellular scale using a high-magnification  
202 objective (100×). Cells were loaded into the chambers as described above and observed after the  
203 establishment of a quasi-steady state (starting 10 h after the chamber was filled with cells, Supplementary  
204 Figure 4). We observed the formation of different landscapes of gene expression for each of the seven  
205 transporters, each with marked territories of low and high expression (Figure 2; Methods). In particular,  
206 HXT1 and HXT7 displayed inversely correlated landscapes of gene expression (*e.g.*, Figure 2a, 2g for 2%  
207 *w/vol* glucose). Both patterns demonstrate the formation and maintenance of a glucose gradient that emerges  
208 from cellular metabolic activity. HXT1 is a low-affinity glucose transporter mainly expressed under high-  
209 glucose conditions, while HXT7 is a high-affinity glucose transporter expressed under low-glucose  
210 conditions only (Figure 2b, 2f). Concomitantly, HXT1 was expressed at the highest levels in the cells close  
211 to the chamber opening (*i.e.*, in the highest glucose concentration), while HXT7 expression peaked further  
212 away in the chamber, indicating a transition to a low-glucose region. We examined the cells at higher  
213 magnification (60×) to assess the localisation of HXT7 gene expression. As expected, in the cells expressing  
214 the highest levels of this gene, the fluorescence was localized to the cell membrane, indicating HXT7 played  
215 an active role in glucose transport in these cells. In contrast, deeper in the colony, we observed lower levels  
216 of HXT7 fluorescence due to the long lifetime of GFP-fused proteins and absence of dilution through cell  
217 division, though this fluorescence was localized in vacuoles, indicating the transporter had been targeted  
218 for degradation by the cells<sup>33</sup> (Figure 2a). Assuming the observed peak of HXT7 fluorescence matches the  
219 peak fluorescence observed in batch culture at a glucose concentration of 0.016% *w/vol*. (Figure 2b, 3), we  
220 could locate the position in the yeast monolayer at which the glucose concentration reached 0.016% *w/vol*.  
221 This position was around  $H_f \sim 450 \mu\text{m}$  from the front, in good agreement with the transition in cell motion  
222 (Figure 1,  $H_m \sim 400 \mu\text{m}$ ).



223

**Figure 2. Landscapes of gene expression self-emerge in extended yeast monolayers.** **2a.** Expression profile of HXT7-GFP along the chamber (average fluorescence levels,  $n=9$ ; standard deviation shown as the envelope) for an external concentration of 2% *w/vol* glucose. Membrane localization of HXT7 was only observed in the cells surrounding the area of peak HXT7 expression, localized at  $\sim 500 \mu\text{m}$  at 2% *w/vol* glucose. **2b.** FACS measurements of HXT7-GFP expression in batch culture (average of three replicates) showing a single intensity peak at  $C_0 = 0.016\%$ . This peak value can be mapped back to the spatial landscape of **2a** to infer the glucose concentration in the region of peak HXT7-GFP fluorescence.  $n=3-6$  per glucose concentration **2c.** On varying the glucose concentration in the nutrient channel, we observed a transition in peak HXT7-GFP fluorescence within the 2D colony. At a concentration of 4% *w/vol* and above, the peak was located close to the dead end of the chamber or not visible, indicating sufficient glucose was available throughout the chamber (color code normalized to maximal expression level). Data obtained by from  $n=8-17$  replicates per glucose concentrations. **2d.** Compared with **2b**, it is possible to roughly define areas of glucose presence in the monolayer for a range of glucose concentrations ( $n=8-17$ , per glucose concentrations, error bars denote  $\pm$  one standard deviation). **2e.** Landscape of HXT1-GFP gene expression over a range of glucose concentrations (color code normalized to maximal expression);  $n=8-9$  per glucose concentrations. **2f.** FACS measurements of HXT1-GFP over a range of glucose concentrations;  $n=3$  replicates. **2g.** Overlay of HXT1 (red) and HXT7 (green) gene expression landscapes at three external glucose concentrations, showing that the expression landscapes of these transporters were inversely correlated, in agreement with their different glucose-dependent expression patterns (compare **2b** and **2f**).

224

225 **Gene expression landscapes depend on the glucose source concentration.** Increasing the glucose  
 226 concentration in the nutrient channel changed the gene expression landscape of all seven glucose  
 227 transporters (Figure 2, 3). In particular, at 1% *w/vol* glucose, HXT1 was only expressed at low levels at the

228 growing front of the colony ( $y < 60 \mu\text{m}$ ). In contrast, at the highest glucose concentration (8% *w/vol*; Figure  
229 2e), HXT1 was expressed at high levels throughout the whole colony, demonstrating glucose was available  
230 throughout the chamber. As HXT1 is mainly expressed under high-glucose conditions ( $> 1\% \text{ w/vol}$  glucose)  
231 in batch culture, this observation indicated the glucose penetration distance (within the chamber) increased  
232 with the external glucose concentration. This is in agreement with the increase in local velocity with the  
233 external glucose concentration in Figure 1, with the size of the growing area also increasing with the  
234 external glucose concentration.

235  
236 In contrast, HXT7 exhibited a peak-like expression pattern, and was repressed under both high-glucose  
237 conditions and when no glucose was present. At low-glucose concentrations (0.1% *w/vol*), a peak in HXT7  
238 expression was observed at the very beginning of the colony ( $y \sim 20 \mu\text{m}$ ), indicating glucose was quickly  
239 absorbed by the cells closest to the chamber opening, thus these were the only cells with access to sufficient  
240 carbon resources to grow and divide. The peak of HXT7 expression moved deeper into the colony as the  
241 glucose concentration increased and disappeared completely at 8% *w/vol* glucose, again indicating  
242 sufficient glucose could diffuse to the end of the chamber under high-glucose conditions (Figure 2, 3).

243  
244 **Reconstructing glucose concentration landscapes using glucose transporter gene expression levels.**

245 We assessed the expression profiles of HXT1-7 in batch culture as a function of glucose concentration (see  
246 *Methods*) to obtain a qualitative idea of the glucose concentrations within the microfluidic device. The data  
247 for HXT7 was particularly revealing: its rather sharp, well-defined expression peak at 0.016% *w/vol*  
248 allowed to define the distance in the microfluidic device at which the glucose concentration is close to that  
249 value (Figure 2a, c). This concentration boundary separates the yeast monolayer into two regions with  
250 different properties, *i.e.*, actively dividing and growth arrest. The position of this boundary moved deeper  
251 into the colony as the external glucose concentration increased (Figure 2d).

252  
253 We extended this idea further and used the complete HXT7 expression profile to infer the glucose  
254 concentrations at all positions within the chambers. Assuming that the local level of HXT7

255 expression is only set by the local glucose concentration, we can use batch culture measurements  
256 of HXT7 expression (based on flow cytometry) to determine the glucose concentration at a given  
257 chamber position (Figure 3c, 3d). However, this only allows us to reconstruct the glucose  
258 concentration gradient up to 0.016% *w/vol.*, *i.e.* in the domain where cells are actively dividing.  
259 The idea is simply to linearly map the two sets of measurements (in batch culture and in the  
260 microfluidic device) based on the fluorescence levels that correspond to the maxima  $F_{max}$  and  $F'_{max}$   
261 and HXT7-GFP fluorescence levels at the chamber entry  $F_0$  and  $F'_0$ . Using the data for HXT7 in  
262 Figure 2, we were able to reconstruct the glucose gradient for different initial glucose  
263 concentrations (Figure 3e). When applied to HXT1, the same inference led to very similar results  
264 (Figure 3f). In both cases, glucose concentrations decay very quickly moving away from the  
265 chamber opening and then exhibit a relatively long tail moving deeper into the colony.

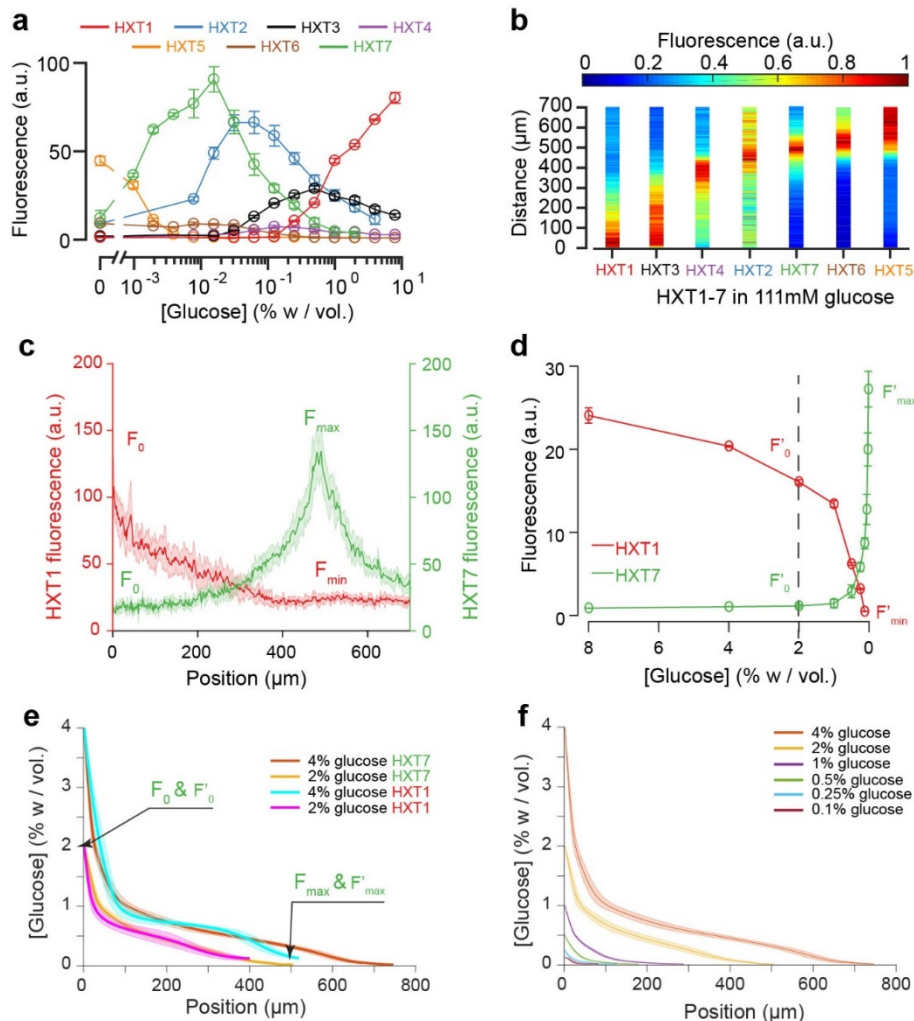


**Figure 3. Using the fluorescence landscapes of glucose transporter gene expression to infer glucose concentration gradients.** **3a.** FACS measurements for HXT1-GFP to HXT7-GFP in batch culture over a range of glucose concentrations. The expression levels of each HXT show a specific dependence on glucose concentration (n=3-6 replicates per glucose concentration). **3b.** Landscapes of gene expression for all HXTs-GFP at an external glucose concentration of 2% w/vol. HXTs are ordered by their relative glucose specificity: HXT1 is expressed under high-glucose conditions, while HXT5 is only expressed at very low-glucose conditions. Assuming a progressive spatial decay in the glucose concentration away from the chamber opening, all maps of gene expression are in perfect agreement with the intensity profiles observed in batch culture (n=8-10 replicates per glucose concentration). **3c-d.** Method of glucose gradient reconstruction. The fluorescence landscape of HXT7 (*resp.* HXT1) shows a peak  $F_{max}$  (*resp.* a minimum,  $F_{min}$ ) at a given location. The fluorescence intensity at the opening of the chamber,  $F_0$ , corresponds to the external glucose concentration,  $C_0$ . Using the FACS measurements of HXT7 (*resp.* HXT1) as a function of glucose concentration, one can define the concentration of glucose that matches the peak  $F_{max}$  (respectively to the minimum  $F_{min}$ ), and the fluorescence intensity that corresponds to  $C_0$ . This allows us to linearly map all other fluorescence intensities for a given glucose concentration from the batch culture to the fluorescence intensities inside the colony, allowing the glucose concentration across the entire cellular monolayer to be reconstructed. Data comes from previously mentioned HXT1 and HXT7 microfluidics and flow cytometry measurements. **3e-f.**

266 **Gene expression landscapes of other genes and transcription factor activity confirm the inferred**  
 267 **glucose gradients.** The fact the seven glucose transporters exhibited varied, robust spatial expression  
 268 patterns under identical conditions (*e.g.*, Figure 3a), together with the observed growth rate landscapes  
 269 (Figure 1), suggests cellular metabolic state varies significantly across the longitudinal axis of the yeast



270 monolayers. This variation was further assessed by mapping the expression and localisation of additional  
271 key genes involved in glucose metabolism.

272

273 MIG1 is a key transcription factor involved in glucose repression that localizes to the nucleus in the  
274 presence of glucose, to repress genes that participate in parallel carbon metabolic pathways (*e.g.*, galactose).

275 Observing the cells at high magnification, we quantified the distance after which MIG1 fluorescence was  
276 not present in the nucleus of the cells (Figure 4b). This distance, around 400  $\mu\text{m}$  at  $C_0 = 2\% w/vol$  glucose,  
277 was in excellent agreement with the data obtained by HXT7 profiling. Interestingly, the spatial transition  
278 from nuclear MIG1 to cytoplasmic MIG1 localisation was very sharp and occurred over just a few cells.

279

280 In agreement with the batch culture observations, we found HXT5 was only expressed in regions with very  
281 low or no glucose concentrations where the cells did not seem to divide over several hours (Figure 4a).

282 Therefore, HXT5 appears to be an excellent marker of growth arrest in this context<sup>34</sup>.



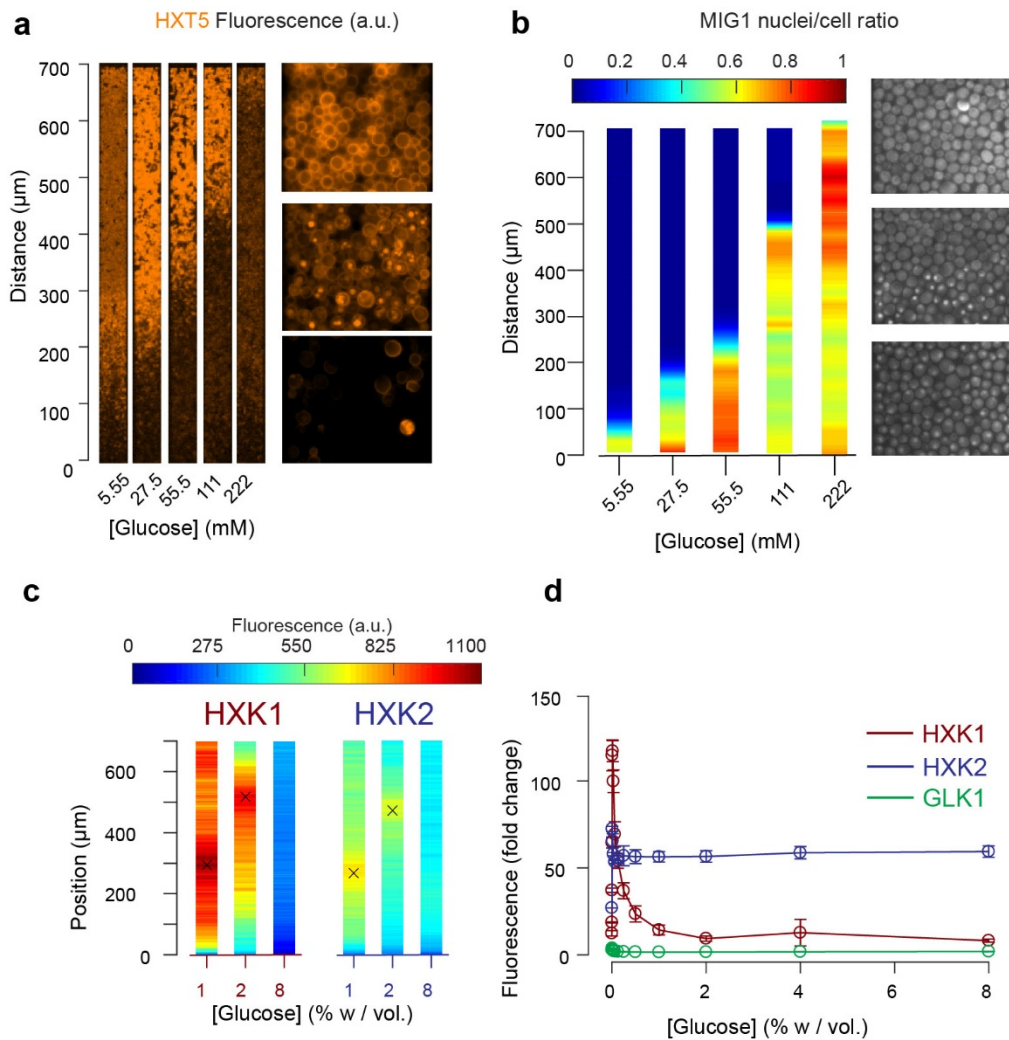


**Figure 4: Other landscapes of genes involved in glucose metabolism. 4a.** Landscape of HXT5 expression. HXT5 is expressed under very low and no glucose conditions and appears to be a good marker of growth arrest. At  $C_0 = 2\%$  *w/vol*, HXT5 expression is in good agreement with the observed absence of cellular division (see Figure 1). **4b.** Landscape of MIG1 activity. MIG1 fluorescence was located in the nucleus in the presence of glucose, with a sharp transition in nuclear localization observed (middle picture, at  $2\%$  *w/vol* glucose in the nutrient channel), confirming the existence of a glucose gradient ( $n=3$  replicates). Total number of cells and cells with nuclear localization of fluorescence were annotated manually and binned into  $25\ \mu\text{m}$  bins. **4c.** HXK1 and HXK2 are hexokinases involved in glucose metabolism. Their landscape of expression exhibited peaks that indicate a transition from high to very low glucose levels ( $n=8-9$  replicates per glucose concentration). **4d.** FACS measurements of HXK1 and HXK2 expression over a range of glucose concentrations ( $n=3-6$  replicates per glucose concentration).

283

284 The expression landscapes of two hexokinases involved in glucose metabolism, HXK1 and HXK2 (Figure

285 4c) that are expressed when cells are grown on non-glucose carbon sources, were also consistent with the

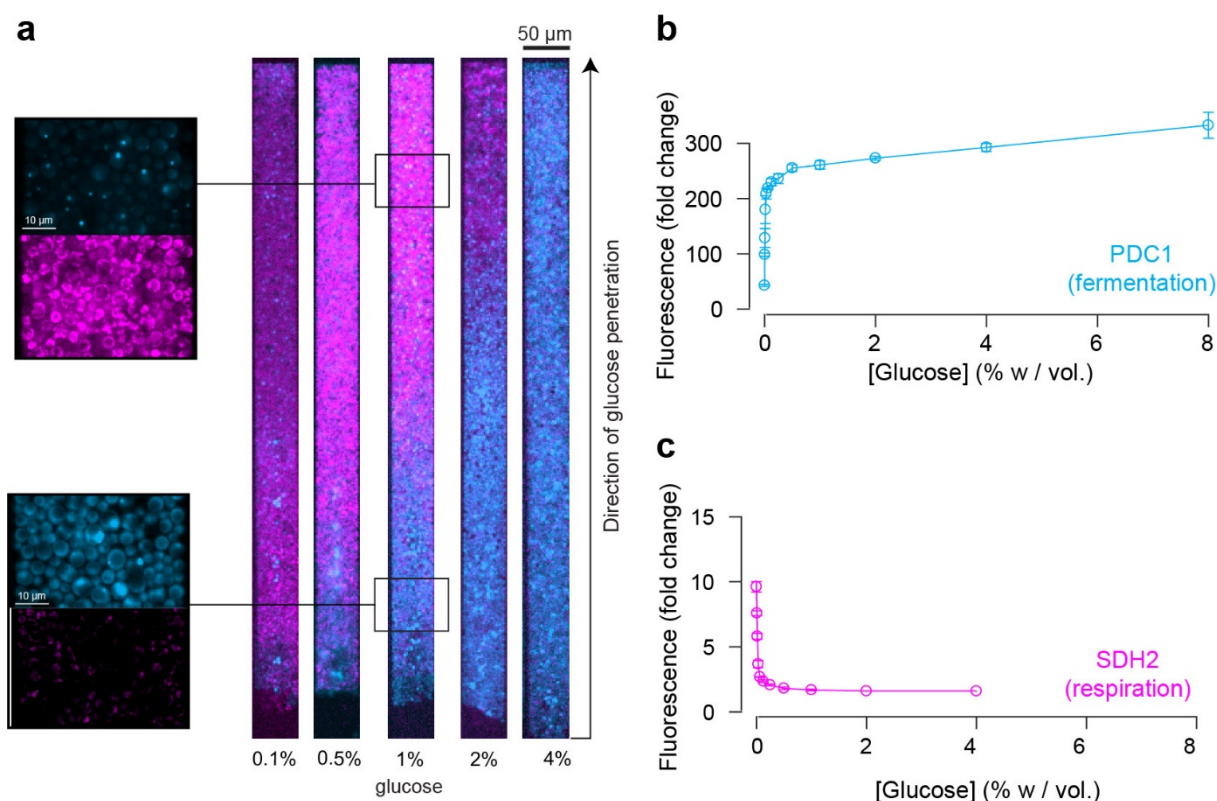
286 batch measurements (Figure 4d, Supplementary Figure 5) and further validated the existence of a glucose

287 gradient. For each profile, we extracted the position of maximal expression and inferred the glucose

288 concentration at this position from the FACS measurements of batch cultures. The batch measurements

289 indicated maximal HXK1 and HXK2 expression were observed at a glucose concentration of about  $0.016\%$

290 *w/vol*. As expected, neither enzyme was expressed at very high glucose concentrations. The HXK1 and  
291 HXK2 expression maxima were similar at the two other glucose concentrations studied, around 300  $\mu\text{m}$  at  
292  $C_0 = 1\%$  and 500  $\mu\text{m}$  at 2% *w/vol*. Again, these data are in very good agreement with the positions of HXT7  
293 peak expression at the same glucose concentrations.  
294  
295 Finally, we examined the expression of PDC1 and SDH2, which are overexpressed in fermenting and  
296 respiring cells, respectively. Their expression landscapes were inversely correlated (Figure 5a), indicating  
297 a transition from fermentative metabolic activity at the nutrient front of the colony to respiratory metabolic  
298 activity towards the dead end of the chamber where glucose is scarce. These expression maps are in good  
299 accordance with our previous results (Figure 1, 2, 4) and the levels of PDC1 and SDH2 expression in batch  
300 culture (Figure 5b, 5c).



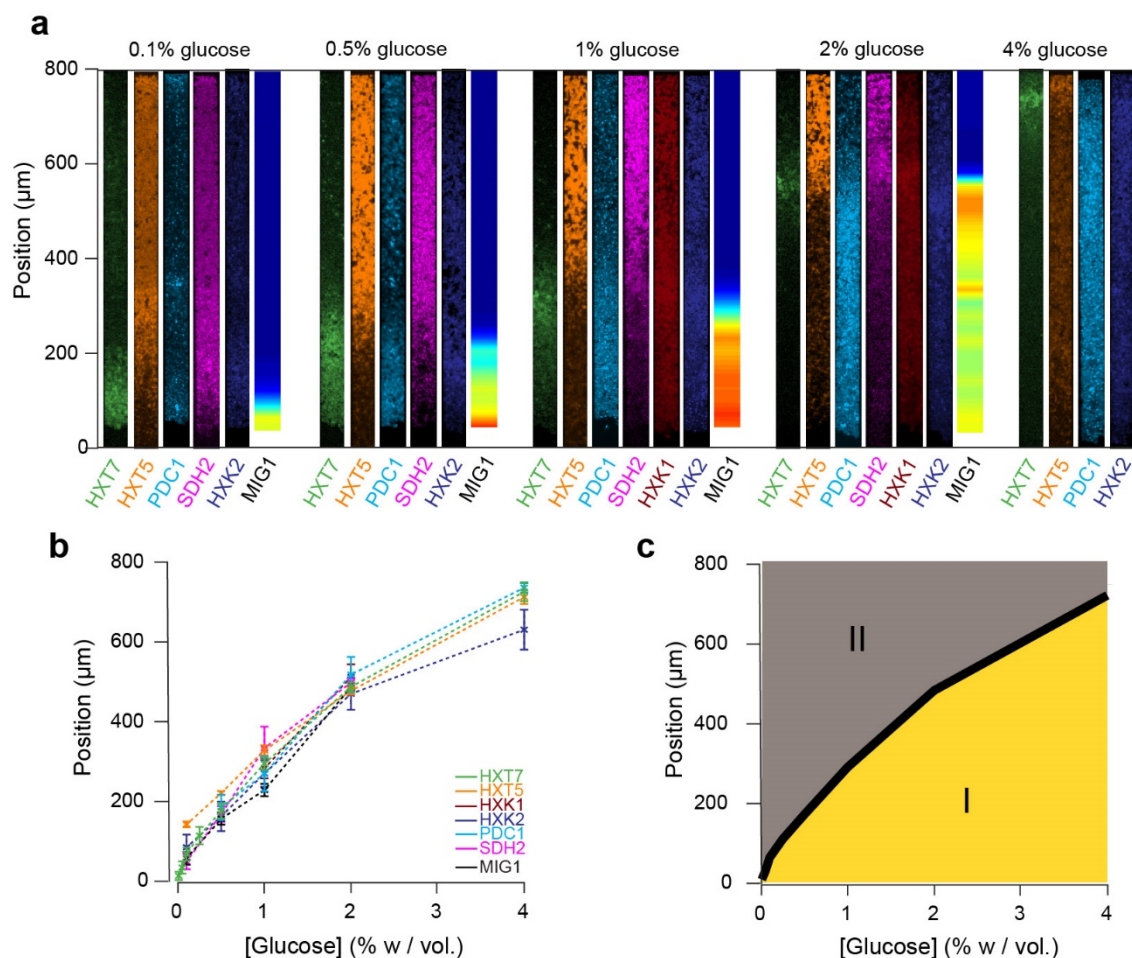
301

**Figure 5. Impact of the glucose gradient on yeast physiology and the emergence of a landscape of phenotypes.** **5a.** Overlay of the landscapes of gene expression of PDC1 (blue) and SHD2 (pink). PDC1 is known to be expressed when yeast cells ferment, SDH2 is mainly expressed in respiring cells. **5b.** FACS measurements of PDC1 expression over a range of glucose concentrations in batch culture (n=3). **5c.** FACS measurements of SDH2 expression over a range of glucose concentrations in batch culture. Taken together, the observed inverse correlation between PDC1 and SDH2 expression in batch culture translate into the emergence of inversely correlated spatial expression patterns within yeast cell monolayers (n=3).

302  
303  
304 **Multiple gene expression landscapes are spatially correlated.** We decided to compare the landscapes of  
305 gene expression for the entire set of reporter genes by aligning the different landscapes across varied  
306 nutrient conditions (Figure 6a). Strikingly, all landscapes showed a high level of spatial correlation. Two  
307 major landscapes emerged: peaking (*e.g.*, HXT7) and switching (*e.g.*, HXT1 or MIG1). We defined and  
308 extracted the typical lengths of the peaking and switching landscapes (Figure 6b) and plotted them as  
309 function of the external glucose concentration (Figure 6c). The typical lengths of all of these landscapes for  
310 different reporter genes were remarkably close, despite the fact that we looked at different cellular  
311 components: a transcription factor (MIG1), glucose transporters (HXTs), metabolic enzymes (HXKs) and  
312 metabolic state reporters (SDH2, PDC1). Notably, we gained a global view of gene expression landscapes  
313 and their interrelationships along a monolayer colony. All data showed the colonies were structured into  
314 two regions with very different properties (Figure 6d): an actively growing region, where cells divide  
315 abundantly and ferment glucose, and a quiescent area, where cells do not divide much and have switched  
316 to respiratory metabolism to compensate for the very low glucose availability. While it is not surprising to  
317 see the expression levels of metabolic genes vary with the glucose concentration, our approach  
318 demonstrates genetic programs not only allow individual cells to adapt to changes in the nutrient  
319 environment, but also enable multicellular assemblies to self-organize spatially through long-range  
320 metabolic interactions. This sheds new light on the coordinated actions of these genes in a biologically  
321 relevant multicellular context that has impact on ecology, evolution, development and emergence of  
322 multicellularity.

323  
324 **Overall, we studied how cells within a monolayer colony collectively shape their microenvironment**  
325 **through long-range metabolic interactions. This is a complex process, in which cells adapt locally,**  
326 **and shape a spatial landscape of gene expression as a global phenotype. As a whole, the structure of**  
327 **an assembly of cells and the microenvironment landscapes emerge as the result of local cellular**  
328 **metabolic activity.**

329



330

**Figure 6: Global view of the emergence of landscapes of gene expression.** **6a.** The different landscapes of gene expression presented in this study are aligned, regrouped and displayed over a range of glucose concentrations. This simple view sheds light on the macroscopic spatial correlations between these different landscapes, which are both setting and traces of the establishment of glucose gradients. **6b.** For each gene expression landscape, we identified the fluorescence peak (HXT7, HXK1, HXK2) or the position of the transition between low and high expression (HXT1, HXT5, SDH2, PDC1) or activity of the transcription factor (MIG1). **6c.** Landscapes of gene expression delimit two regions in which cells are physiologically different. Phase I indicates active growth by fermentation in the presence of glucose; Phase II indicates growth arrest or very limited growth via respiratory metabolism at zero or close to zero glucose concentrations. The transition between the two phases typically takes place relatively sharply, over a hundred micrometers or  $\sim 20$  cells.

331

## 332 Discussion

333 Here, we took an alternative point of view compared to traditional systems and single-cell biology. Rather  
334 than studying single-cell metabolic properties in a well-mixed, homogeneous environment, we designed a  
335 microfluidic chip to force yeast cells to grow and shape their microenvironment, solely by fixing the

336 properties of the microenvironment at the boundary of the monolayer. This approach allowed us to  
337 simultaneously measure properties on both the single-cell-scale and structured population-scale and holds  
338 potential for establishing a quantitative link between these scales.

339  
340 Specifically, we showed that cells self-generate nutrient landscapes that in turn influence cellular  
341 metabolism and gene expression profiles. This behaviour, based on nutrient uptake adaptation, is generic  
342 and feeds back on the behaviour of other cells through what we call non-specific long-range metabolic  
343 interactions. Indeed, the microenvironment sensed by cells a few hundred micrometres inside a colony is  
344 very different from the microenvironment experienced by external cells. Notably, gradients emerge over  
345 relatively short distances, and this process may possibly affect studies of cellular populations within  
346 microfluidics settings. More importantly, quantitative description of gene expression maps is critical if one  
347 wants to understand the establishment and behaviour of cellular communities, whether these are as simple  
348 as yeast colonies or more complex, such as biofilms and complex microbial ecosystems in which several  
349 types of cells cohabit and interact. Indeed, in addition to the described long-range metabolic interactions,  
350 many other environmental and genetic determinants such as intercellular communication, cell surface  
351 properties, cell-cell adhesion strength and secretion of extracellular matrix components have been shown  
352 to participate in the emergence of the complex morphology<sup>3,35,36</sup> and internal structure of microbial colonies  
353 in such complex situations. The nature of many of these interactions could also be studied using similar  
354 microfluidic devices to identify the relative contribution and relationship of environmental and genetic  
355 determinants to the metabolically generated microenvironment.

356  
357 Even in a simple situation such as the monolayers studied here, it is not straightforward to infer the spatial  
358 structure of the microenvironment from single-cell knowledge. A proper model should take into account  
359 how the growth rate and specific absorption rate vary with the glucose concentration and the  
360 microenvironment. Modelling the entire complexity of the microenvironment is hardly possible, even  
361 today. Thus, we decided to take a different approach and use key genes involved in glucose metabolism to  
362 infer the glucose concentration gradient. We showed that different reporter genes consistently reported the



363 same glucose gradient. We envision that the data extracted from relevant fluorescent reporters could be fed  
364 into agent-based or mean-field models that take cell-cell interactions, mechanics and spatial diffusion of  
365 metabolites into account to fill the gap between data generated from single cells to data that is relevant to  
366 evolution and ecology, *i.e.* at the colony scale. We anticipate that linking local properties to macroscopic,  
367 global behaviour will help to understand the architecture of microbial communities and how evolution  
368 shapes the development of these architectures through long-range metabolic interactions.

369  
370 Furthermore, while the spatial microenvironment is not fully characterized, we have shown the emergence  
371 of gradients, and simultaneously gene expression landscapes, are robust and reproducible features of the  
372 colony. Moreover, the landscapes can be compared to extract correlation patterns and infer how gene  
373 regulatory networks act in synchronicity to establish the microenvironment within the colony. This  
374 approach may provide a relatively simple, yet effective method of screening for “organismic” properties  
375 that have been shaped by evolution and are only relevant in a multicellular context.

376  
377 Our future efforts to extend the application of this setup will be dedicated to the study of how the  
378 microenvironment dynamically changes when external conditions are altered, an uncharted territory at the  
379 scale of a multicellular assembly that is central to the understanding of microbial ecosystem resistance to  
380 stress, environmental fluctuations and adaptation. **We anticipate that similar approaches could be used**  
381 **to study aging, cooperation and competition, cell memory or evolutionary dynamics, as well as**  
382 **quantitative characterization of (synthetic) ecological systems and mixtures of cells relevant to**  
383 **ecology and chemical biology.**

384

385

## 386 Materials and Methods

387 **Yeast strains.** All experiments were performed using haploid *S. cerevisiae* strains derived from the S288C  
388 background - BY4741: *MATa his3Δ1 leu2Δ0 met15Δ0 ura3Δ0*. See Supplementary Table T1 for a detailed  
389 list of the yeast strains used in this study.

390  
391 **Microscopy.** We used an inverted fluorescence microscope (IX81, Olympus) equipped with an EMCCD  
392 camera (Evolve 512, Photometrics) and X-Cite exacte fluorescence light source (Lumen Dynamics).  
393 Optical filters from Chroma Technology Corporation ET-EGFP (U-N49002; Ex 470/40nm Di495 Em  
394 525/50nm) and ET-DsRed (U-N49005; Ex 545/30nm Di570 Em620/60nm) were used to observe GFP and  
395 RFP fluorescence. Cells were observed using Olympus 10× (Plan 10x / 0.25 NA), 60× (PlanApo N 60x /  
396 1.42 NA Oil) and 100× (UPlanFL N 100x / 1.3 NA Oil) objectives. Open-source  $\mu$ Manager<sup>37</sup> microscopy  
397 software was used to control all of these components and setup multi-dimensional acquisition. The  
398 temperature inside the microscope incubation chamber that contained the media and cells was maintained  
399 at 30 °C (Life Imaging Services). Fluorescence intensity was set to 10% of maximum output, fluorescence  
400 exposure was set to 1000 ms and camera gain was set at maximum. The time interval between each  
401 acquisition cycle was 6 min.

402  
403 **Microfluidics and cell loading.** Microfluidic devices were constructed using soft lithography techniques.  
404 Photomasks were drawn using L-Edit software (Tanner) and printed on a high-resolution glass substrate  
405 (Delta Mask). A master wafer was created using SU-8 2000 (MicroChem) epoxy-based photoresist that  
406 was spin-coated to the appropriate thickness and exposed to UV light using an appropriate photomask to  
407 create the desired pattern. Multi-layered patterns were aligned and exposed to UV light using a MJB4  
408 manual mask aligner (SUSS MicroTec) and the dimensions of the master wafer were checked using a  
409 Dektak 150 surface profiler (Veeco). The master wafer was treated with 95% (3-mercaptopropyl)-  
410 trimethoxysilane (Sigma) for 1 h in the vapour phase. Microfluidic chips were created by casting a degassed  
411 10:1 mix of polydimethylsiloxane (PDMS) and curing agent (Sylgard 184 kit; Dow Corning) on the master  
412 wafer, followed by at least 2 h curing at 65 °C. Each chip was gently cut and peeled off the master wafer;



413 the entry/exit ports were punched out. The chip and a glass coverslip (24 x 50 mm #1; Menzel-Gläser) were  
414 treated with O<sub>2</sub> plasma for 1 min in a plasma cleaner (Harrick Plasma), bonded together and incubated at  
415 65 °C for 10 min. Before loading cells, the chips were coated with 1% Pluronic F-127 (Sigma) for 30 min.  
416 Cells were precultured overnight in 5 mL of synthetic complete (SC) medium containing 2% *w/vol* glucose  
417 in a shaking incubator at 30 °C, diluted 50-fold into 50 mL of SC + 2% *w/vol* glucose, cultured for 5-6 h in  
418 a shaking incubator at 30 °C to an OD<sub>600</sub> of 0.2-0.4, collected by centrifugation, and loaded into the  
419 microfluidic system with a pipette. The microfluidic system was centrifuged for 2 min at 1000 rpm using  
420 3D-printed adaptors (Laurell WS-650 spin coater) to force the cells into the dead-end cell chambers. Liquid  
421 media was flowed rapidly through the flow channel to remove excess cells and the flow rate was set to 5  
422 µL/min. A pressure-based microfluidic flow control system (MFCS; Fluigent) coupled with a flow rate  
423 platform (Fluigent) and a flow rate control module (Fluigent) that measured the flow rate and kept it  
424 constant by adjusting the pressure through a feedback loop was used to push liquid media through the flow  
425 channel. The output was kept at a constant pressure of 100 mbar above atmospheric pressure to minimize  
426 formation of air bubbles inside the flow channel.

427  
428 **Flow cytometry.** Flow cytometry experiments were performed on a Gallios Flow Cytometer (Beckman  
429 Coulter) using a 488 nm excitation laser and 530/30 nm FL1 emission filter to detect GFP fluorescence.  
430 Data analysis was performed using Kaluza Flow Cytometry Analysis Software (Beckman Coulter).  
431 Approximately 10<sup>4</sup> cells were inoculated in 10 mL of SC medium containing various glucose concentrations  
432 (log<sub>2</sub> dilutions from 8% to 0.0078125%, and 0% *w/vol* glucose) and cultured in a shaking incubator at 30  
433 °C to an OD<sub>600</sub> of ~0.02-0.2 depending on the starting glucose concentration. Cells were then diluted 10-fold  
434 into 10 mL of fresh SC media containing the same starting glucose concentration and grown for 4-5 h in a  
435 shaking incubator at 30 °C, centrifuged at 4000 rpm for 10 min, re-suspended in 300 µL of PBS pH 7.4  
436 buffer (Gibco) and fluorescence was measured using the flow cytometer. The supernatant of each sample  
437 was collected, and the glucose concentration was measured using the Glucose (HK) Assay Kit (Sigma) to  
438 confirm the glucose concentration remained constant during the growth phase.

439

440 **Image analysis.** Image analysis was performed using open-source ImageJ software<sup>38</sup>. To obtain front  
441 velocity, we applied a threshold (Otsu) to detect the bottom frontier over time after flattening the  
442 background using a FFT band-pass filter. To compute the local speed of the cells inside the cell assembly,  
443 we used the plugin TrackMate<sup>39</sup> to track cell trajectories.

444

## 445 Acknowledgments

446 The authors would like to thank Sébastien Léon (IJM, CNRS) and their respective team members for their  
447 critical reading of this manuscript. This work was supported by the *Agence Nationale de la Recherche*  
448 (ICEBERG-ANR-10-BINF-06-01; ANR-16-CE12-0025-01), the interdisciplinary program of the  
449 *University Sorbonne Paris Cité*, the *Who am I?* Laboratory of Excellence (ANR-11-LABX-0071 and ANR-  
450 11-IDEX-0005-01) and the European Research Council (ERC) under the European Union's Horizon 2020  
451 research and innovation programme (grant agreement No 724813).

## 452 Author Contributions

453 ZSM performed all experiments; ZSM, MA, ABL, PH analysed the data; ZSM, XS performed image  
454 analysis; ZSM, ABL, PH designed the experiments and wrote the manuscript with contributions from CV  
455 and JMdM.

## 456 Supplementary Information

457 Supplementary information contains five figures, one supplementary table and one supplementary movie.

458

## 459 References

- 460 1. Vulin, C. *et al.* Growing Yeast into Cylindrical Colonies. *Biophys. J.* **106**, 2214–2221 (2014).
- 461 2. Čáp, M., Štěpánek, L., Harant, K., Váchová, L. & Palková, Z. Cell Differentiation within a Yeast  
462 Colony: Metabolic and Regulatory Parallels with a Tumor-Affected Organism. *Mol. Cell* **46**, 436–448  
463 (2012).
- 464 3. Nadell, C. D., Drescher, K. & Foster, K. R. Spatial structure, cooperation and competition in biofilms.  
465 *Nat. Rev. Microbiol.* **14**, 589–600 (2016).
- 466 4. Carmona-Fontaine, C. *et al.* Emergence of spatial structure in the tumor microenvironment due to the  
467 Warburg effect. *Proc. Natl. Acad. Sci.* **110**, 19402–19407 (2013).
- 468 5. Delarue, M. *et al.* Compressive Stress Inhibits Proliferation in Tumor Spheroids through a Volume  
469 Limitation. *Biophys. J.* **107**, 1821–1828 (2014).
- 470 6. Shapiro, J. A. Thinking about bacterial populations as multicellular organisms. *Annu. Rev. Microbiol.*  
471 **52**, 81–104 (1998).
- 472 7. Shou, W., Ram, S. & Vilar, J. M. G. Synthetic cooperation in engineered yeast populations. *Proc. Natl.*  
473 *Acad. Sci. U. S. A.* **104**, 1877–1882 (2007).
- 474 8. Xavier, J. B. & Foster, K. R. Cooperation and conflict in microbial biofilms. *Proc. Natl. Acad. Sci.*  
475 **104**, 876–881 (2007).
- 476 9. H. Koschwanez, J., R. Foster, K. & W. Murray, A. Sucrose Utilization in Budding Yeast as a Model  
477 for the Origin of Undifferentiated Multicellularity. *PLoS Biol.* **9**, e1001122 (2011).
- 478 10. Palková, Z. & Váchová, L. Life within a community: benefit to yeast long-term survival. *FEMS*  
479 *Microbiol. Rev.* **30**, 806–824 (2006).
- 480 11. Antwis, R. E. *et al.* Fifty important research questions in microbial ecology. *FEMS Microbiol. Ecol.*  
481 **93**, (2017).
- 482 12. Gonzalez, A. *et al.* Characterizing microbial communities through space and time. *Curr. Opin.*  
483 *Biotechnol.* **23**, 431–436 (2012).
- 484 13. Widder, S. *et al.* Challenges in microbial ecology: building predictive understanding of community  
485 function and dynamics. *ISME J.* **10**, 2557–2568 (2016).

- 486 14. Bryers, J. D. Medical Biofilms. *Biotechnol. Bioeng.* **100**, 1–18 (2008).
- 487 15. Gilbert, J. A. *et al.* Current understanding of the human microbiome. *Nat. Med.* **24**, 392–400 (2018).
- 488 16. Estrela, S. & Brown, S. P. Community interactions and spatial structure shape selection on antibiotic  
489 resistant lineages. *PLOS Comput. Biol.* **14**, e1006179 (2018).
- 490 17. Ratcliff, W. C., Denison, R. F., Borrello, M. & Travisano, M. Experimental evolution of  
491 multicellularity. *Proc. Natl. Acad. Sci. U. S. A.* **109**, 1595–600 (2012).
- 492 18. Nadell, C. D., Foster, K. R. & Xavier, J. B. Emergence of spatial structure in cell groups and the  
493 evolution of cooperation. *PLoS Comput. Biol.* **6**, e1000716 (2010).
- 494 19. Kim, H. J., Boedicker, J. Q., Choi, J. W. & Ismagilov, R. F. Defined spatial structure stabilizes a  
495 synthetic multispecies bacterial community. *Proc. Natl. Acad. Sci.* **105**, 18188–18193 (2008).
- 496 20. Bennett, M. R. & Hasty, J. Microfluidic devices for measuring gene network dynamics in single cells.  
497 *Nat. Rev. Genet.* **10**, 628–638 (2009).
- 498 21. Cookson, S., Ostroff, N., Pang, W. L., Volfson, D. & Hasty, J. Monitoring dynamics of single-cell gene  
499 expression over multiple cell cycles. *Mol. Syst. Biol.* **1**, E1–E6 (2005).
- 500 22. Robert, L. *et al.* Pre-dispositions and epigenetic inheritance in the Escherichia coli lactose operon  
501 bistable switch. *Mol. Syst. Biol.* **6**, 357 (2010).
- 502 23. Ni, M. *et al.* Pre-Disposition and Epigenetics Govern Variation in Bacterial Survival upon Stress. *PLoS*  
503 *Genet.* **8**, (2012).
- 504 24. Llamosi, A. *et al.* What Population Reveals about Individual Cell Identity: Single-Cell Parameter  
505 Estimation of Models of Gene Expression in Yeast. *PLOS Comput. Biol.* **12**, e1004706 (2016).
- 506 25. Jo, M. C., Liu, W., Gu, L., Dang, W. & Qin, L. High-throughput analysis of yeast replicative aging  
507 using a microfluidic system. *Proc. Natl. Acad. Sci.* **112**, 9364–9369 (2015).
- 508 26. Yang, Y. *et al.* Temporal scaling of ageing as an adaptive strategy of Escherichia coli. *bioRxiv* 376566  
509 (2018). doi:10.1101/376566
- 510 27. Wang, P. *et al.* Robust growth of Escherichia coli. *Curr. Biol. CB* **20**, 1099–103 (2010).
- 511 28. Lambert, G. & Kussel, E. Memory and Fitness Optimization of Bacteria under Fluctuating  
512 Environments. *PLoS Genet.* **10**, (2014).

- 513 29. Xu, Z. *et al.* Two routes to senescence revealed by real-time analysis of telomerase-negative single  
514 lineages. *Nat. Commun.* **6**, 7680 (2015).
- 515 30. Pfeiffer, T. & Morley, A. An evolutionary perspective on the Crabtree effect. *Front. Mol. Biosci.* **1**, 17  
516 (2014).
- 517 31. Hagman, A. & Piškur, J. A Study on the Fundamental Mechanism and the Evolutionary Driving Forces  
518 behind Aerobic Fermentation in Yeast. *PLoS ONE* **10**, (2015).
- 519 32. Boyer, D. *et al.* Buckling instability in ordered bacterial colonies. *Phys. Biol.* **8**, 026008 (2011).
- 520 33. Hovsepian, J. *et al.* Multilevel regulation of an  $\alpha$ -arrestin by glucose depletion controls hexose  
521 transporter endocytosis. *J Cell Biol* **216**, 1811–1831 (2017).
- 522 34. Verwaal, R. *et al.* HXT5 expression is determined by growth rates in *Saccharomyces cerevisiae*. *Yeast*  
523 **19**, 1029–1038 (2002).
- 524 35. Granek, J. A. & Magwene, P. M. Environmental and Genetic Determinants of Colony Morphology in  
525 Yeast. *PLOS Genet.* **6**, e1000823 (2010).
- 526 36. Biofilms: an emergent form of bacterial life | Nature Reviews Microbiology. Available at:  
527 <https://www.nature.com/articles/nrmicro.2016.94>. (Accessed: 2nd November 2018)
- 528 37. Edelstein, A. D. *et al.* Advanced methods of microscope control using  $\mu$ Manager software. *J. Biol.*  
529 *Methods* **1**, e10 (2014).
- 530 38. Schneider, C. A., Rasband, W. S. & Eliceiri, K. W. NIH Image to ImageJ: 25 years of image analysis.  
531 *Nat. Methods* **9**, 671–675 (2012).
- 532 39. TrackMate: An open and extensible platform for single-particle tracking - ScienceDirect. Available at:  
533 <https://www.sciencedirect.com/science/article/pii/S1046202316303346>. (Accessed: 2nd November  
534 2018)
- 535